

PAPER • OPEN ACCESS

Level anti-crossings of a nitrogen-vacancy center in diamond: decoherence-free subspaces and 3D sensors of microwave magnetic fields

To cite this article: K Rama Koteswara Rao and Dieter Suter 2020 *New J. Phys.* **22** 103065

View the [article online](#) for updates and enhancements.

New Journal of Physics

The open access journal at the forefront of physics

Deutsche Physikalische Gesellschaft 

IOP Institute of Physics

Published in partnership
with: Deutsche Physikalische
Gesellschaft and the Institute
of Physics



PAPER

OPEN ACCESS

RECEIVED
8 June 2020

REVISED
2 October 2020

ACCEPTED FOR PUBLICATION
13 October 2020

PUBLISHED
30 October 2020

Original content from
this work may be used
under the terms of the
[Creative Commons
Attribution 4.0 licence](#).

Any further distribution
of this work must
maintain attribution to
the author(s) and the
title of the work, journal
citation and DOI.



Level anti-crossings of a nitrogen-vacancy center in diamond: decoherence-free subspaces and 3D sensors of microwave magnetic fields

K Rama Koteswara Rao^{1,2} and Dieter Suter^{1,*}

¹ Fakultät Physik, Technische Universität Dortmund, D-44221 Dortmund, Germany

² Department of Physics, Bennett University, Greater Noida 201310, India

* Author to whom any correspondence should be addressed.

E-mail: Dieter.Suter@tu-dortmund.de

Keywords: NV center, decoherence-free subspaces, ZEFOZ shift, level anti-crossings, coherence times

Abstract

Nitrogen-vacancy (NV) centers in diamond have become an important tool for quantum technologies. All of these applications rely on long coherence times of electron and nuclear spins associated with these centers. Here, we study the energy level anti-crossings of an NV center in diamond coupled to a first-shell ¹³C nuclear spin in a small static magnetic field. These level anti-crossings (LACs) occur for specific orientations of the static magnetic field due to the strong non-secular components of the Hamiltonian. At these orientations we observe decoherence-free subspaces, where the electron spin coherence times (T_2^*) are 5–7 times longer than those at other orientations. Another interesting property at these LACs is that individual transition amplitudes are dominated by a single component of the magnetic dipole moment. Accordingly, this can be used for vector detection of microwave magnetic fields with a single NV center. This is particularly important to precisely control the center using numerical optimal control techniques.

1. Introduction

Nitrogen-vacancy (NV) centers in diamond have many interesting properties for various applications ranging from quantum information processing to nano-scale imaging [1–6]. For most of these applications, long coherence times of electron and nuclear spins associated with the NV center are essential. Dynamical decoupling pulse sequences are effectively used to decouple NV centers from their environment and hence improve the coherence times of the centers [7–15]. For NV centers, the major source of decoherence is the spin bath formed by the electron and nuclear spins of impurity atoms (e.g. substitutional nitrogen) and ¹³C nuclear spins in the diamond lattice [16–18]. The coherence times of NV centers can be significantly extended in ultrapure diamond crystals, where the substitutional nitrogen atom concentration is very low. The ¹³C nuclear spin noise can be reduced by using crystals enriched with ¹²C atoms [19]. However, ¹³C nuclear spins that are strongly coupled to the electron spin of an NV center can also be useful as qubits, either as part of a quantum register [15, 20–23] or for storing quantum information [15, 24, 25]. For example, the ¹³C nuclear spin of the first coordination-shell has a strong hyperfine coupling with the electron spin of the NV center, which can be used to implement fast multi-qubit gates [23, 26]. The disadvantage of using diamond crystals enriched in ¹²C is that these useful qubits are lost.

In this work, we demonstrate that the effect of nuclear spin noise can be reduced substantially by an appropriate choice of the magnetic field such that a decoherence-free subspace is established near a level anti-crossing (LAC) of an NV center. LACs of NV centers that occur between the $m_s = 0$ and $m_s = -1$ spin sublevels of both the ground and optically excited states have been used for various purposes [27–30], such as polarizing the nuclear spins. These anti-crossings occur at magnetic field strengths of ≈ 500 G and ≈ 1000 G. Here, we study LACs, that occur at much smaller field strengths, of an NV center coupled to a first-shell ¹³C nuclear spin. Specifically, we study the LACs that occur at two different magnetic field orientations: (i)

the strength and orientation of the magnetic field are such that the spectral splitting due to the Zeeman interaction of the electron spin is equal to the splitting due to the hyperfine interaction of the first-shell ^{13}C nuclear spin (≈ 127 MHz). (ii) The magnetic field is oriented in the plane perpendicular to the NV axis. This LAC is induced by transverse magnetic field and occurs even in NV centers that are not coupled to a proximal ^{13}C nuclear spin. Close to the LACs, the mixing of the states results in zero first-order Zeeman (ZEFOZ) shift [31–34] of some of the transitions and correspondingly reduced perturbations by magnetic-field noise. This effect manifests itself by long coherence times (T_2^*), almost an order of magnitude longer than at other orientations.

An NV center coupled to a first-shell ^{13}C nuclear spin is particularly attractive for quantum information processing because of the strong hyperfine coupling between the electron and nuclear spins [17, 23, 25, 26]. However, harnessing the full potential of this system requires accurate knowledge of the Hamiltonian. The time-independent internal Hamiltonian of this system has been thoroughly investigated [35–37]. In addition, precise knowledge of the time-dependent microwave (MW) Hamiltonian, including the orientation of the MW field with respect to the center, is also important for precise control of the system. This information is particularly important in such centers, since the first-shell ^{13}C nuclear spin breaks the rotational symmetry of the center. At the LACs discussed above, the transition amplitudes of some of the transitions are dominated by a single component of the magnetic dipole moment. This can be used to determine the strength and orientation of the MW magnetic field with a single NV center. A similar vector detection scheme using NV centers was reported in reference [38]. However, that required at least three NV centers with different orientations in the focal spot of the objective lens.

This paper is structured as follows. In section 2, we discuss the system, its Hamiltonian and the experimental setup. In sections 3 and 4, we analyze the two LACs and discuss the decoherence-free subspaces and the vector detection of MW magnetic fields. Finally, in section 5, we draw some conclusions.

2. System and Hamiltonian

The system of interest here is a single NV center coupled to a first-shell ^{13}C nuclear spin. The probability of finding such a center in a ^{13}C natural abundant diamond crystal is 3.3%. Figure 1(a) shows its structure and defines the coordinate system that we use here. The NV symmetry axis is the z -axis of the center, the x -axis is perpendicular to this axis and lies in the plane containing the vacancy, nitrogen, and the ^{13}C atom, and the y -axis is perpendicular to both of them. The Hamiltonian of the total system consisting of the electron spin ($\mathbf{S} = 1$), the ^{13}C nuclear spin ($\mathbf{I}_1 = 1/2$), and the ^{14}N nuclear spin ($\mathbf{I}_2 = 1$) in this coordinate system can be written as

$$\mathcal{H}_{\text{sys}} = DS_z^2 + \gamma_e \mathbf{B} \cdot \mathbf{S} + \gamma_{n1} \mathbf{B} \cdot \mathbf{I}_1 + \gamma_{n2} \mathbf{B} \cdot \mathbf{I}_2 + PI_{2z}^2 + \mathbf{S} \cdot \mathcal{A}_1 \cdot \mathbf{I}_1 + \mathbf{S} \cdot \mathcal{A}_2 \cdot \mathbf{I}_2. \quad (1)$$

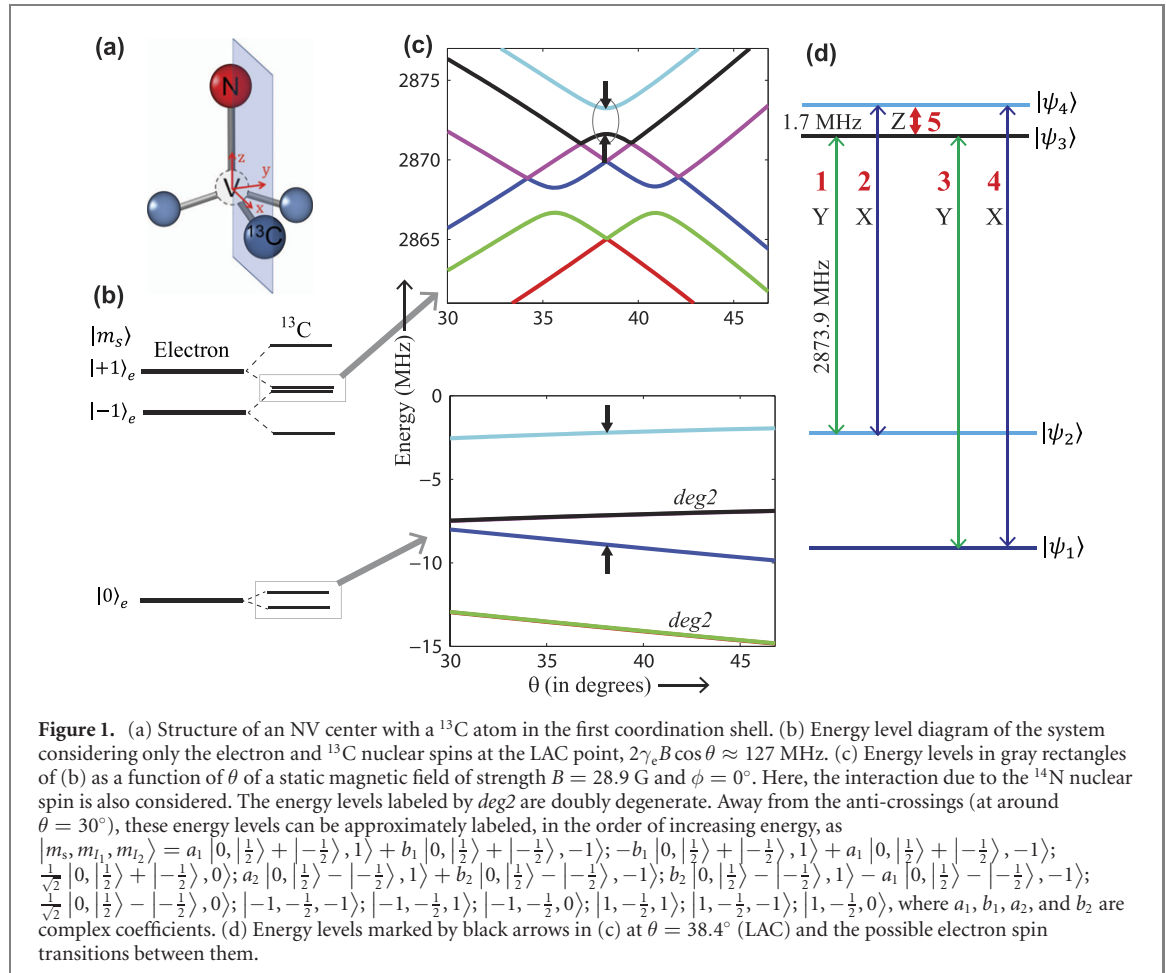
Here, $D = 2.87$ GHz is the electron-spin zero-field splitting, and $\mathbf{B} = B(\sin \theta \cos \phi, \sin \theta \sin \phi, \cos \theta)$ represents the static magnetic field, where θ and ϕ are its polar and azimuthal angles. $P = -4.95$ MHz [39] represents the quadrupolar splitting of the ^{14}N nuclear spin, and \mathcal{A}_1 and \mathcal{A}_2 represent hyperfine tensors of the ^{13}C and ^{14}N nuclear spins respectively with the electron spin. The parameters of the hyperfine tensors are $\mathcal{A}_{1zz} = 128.9$, $\mathcal{A}_{1yy} = 128.4$, $\mathcal{A}_{1xx} = 189.3$, and $\mathcal{A}_{1xz} = 24.1$ MHz [37], and $\mathcal{A}_{2zz} = -2.16$ MHz and $\sqrt{\mathcal{A}_{2xx}^2 + \mathcal{A}_{2yy}^2} = -2.6$ MHz [30, 36, 40, 41].

The Hamiltonian for the coupling of the MW or radio-frequency (RF) field to the electron spin transitions can be written as

$$\mathcal{H}_{\text{mw}} = \sqrt{2} \gamma_e B_{\text{mw}} (\sin \zeta \cos \eta S_x + \sin \zeta \sin \eta S_y + \cos \zeta S_z) \cos(\omega t + \varphi), \quad (2)$$

where B_{mw} , ζ , and η represent the amplitude, polar, and azimuthal angles respectively of the applied field at the site of the NV center. ω and φ represent the frequency and phase of this field.

All the experiments of this work have been performed using a home-built confocal microscope for selective excitation and detection of single NV centers and an MW circuit for resonant excitation of electron spin transitions. A $20\ \mu\text{m}$ thin wire was attached to the diamond surface to generate the MW fields. The used diamond crystal has a natural-abundance ^{13}C concentration and the concentration of substitutional nitrogen centers is < 5 ppb. Studying LACs of the present work requires a precise orientation of the static magnetic field. This was achieved by a permanent magnet attached to two rotational stages such that their axes are orthogonal to each other and cross at the site of diamond crystal. By rotating the magnet with these rotational stages, a 3D rotation of the magnetic field can be achieved. The strength of the magnetic field (B) at the site of the NV center was 28.9 G.



3. Nuclear spin induced LAC

First, consider the LACs that occur in the $m_s = \pm 1$ manifold when the energy level splitting due to the Zeeman interaction of the electron spin ($2\gamma_e B \cos \theta$) is equal to the corresponding splitting due to the hyperfine interaction with the ^{13}C nuclear spin, which is ≈ 127 MHz. These LACs have been recently used to study the strong-driving dynamics of a two-level quantum system beyond the rotating-wave approximation [42]. For the magnetic field of strength 28.9 G, these LACs occur when θ is close to 38.4° . The energy level diagram of the system considering only the electron and ^{13}C nuclear spins at this magnetic field orientation is shown in figure 1(b). The relevant energy levels for the present work are marked by gray rectangles. Figure 1(c) shows these levels on an expanded scale as a function of θ of the static magnetic field. As can be seen from this plot, there are three similar LACs in the $m_s = \pm 1$ manifold when θ is close to 35.7° , 38.4° , and 41.0° . These three LACs correspond to the three states ($m_{I_2} = 1, 0$, and -1) of the ^{14}N nuclear spin. Here, we analyze the LAC that occurs at $\theta = 38.4^\circ$ (marked by the gray oval in figure 1(c)).

At this magnetic field orientation, the four energy levels (two in the $m_s = 0$ manifold and two in the $m_s = \pm 1$ manifold) marked by small black arrows in figure 1(c) are illustrated in figure 1(d). We label the corresponding eigenstates as $|\psi_1\rangle$, $|\psi_2\rangle$, $|\psi_3\rangle$, and $|\psi_4\rangle$. In the $|m_s, m_{I_1}, m_{I_2}\rangle$ basis, they are approximately

$$\begin{aligned} |\psi_{1,2}\rangle &\approx \left|0, \frac{|−1/2\rangle \pm |1/2\rangle}{\sqrt{2}}, 0\right\rangle, \\ |\psi_{3,4}\rangle &\approx \left|\frac{|−1\rangle \mp |1\rangle}{\sqrt{2}}, −\frac{1}{2}, 0\right\rangle. \end{aligned} \quad (3)$$

Between these four energy states, five electron spin transitions are possible, which are shown by double sided arrows. Four of these five transitions (thin green and blue arrows) are between the $m_s = 0$ and $m_s = \pm 1$ manifolds and they fall in the MW region, and the fifth transition (thick red arrow), which falls into the RF region, connects the two states of the $m_s = \pm 1$ manifold. The four MW transitions have long coherence times (T_2^*) compared to magnetic field orientations without LACs. This is because, at the LAC, the first-order derivatives of these transition frequencies (ν_i) with respect to the magnetic field are

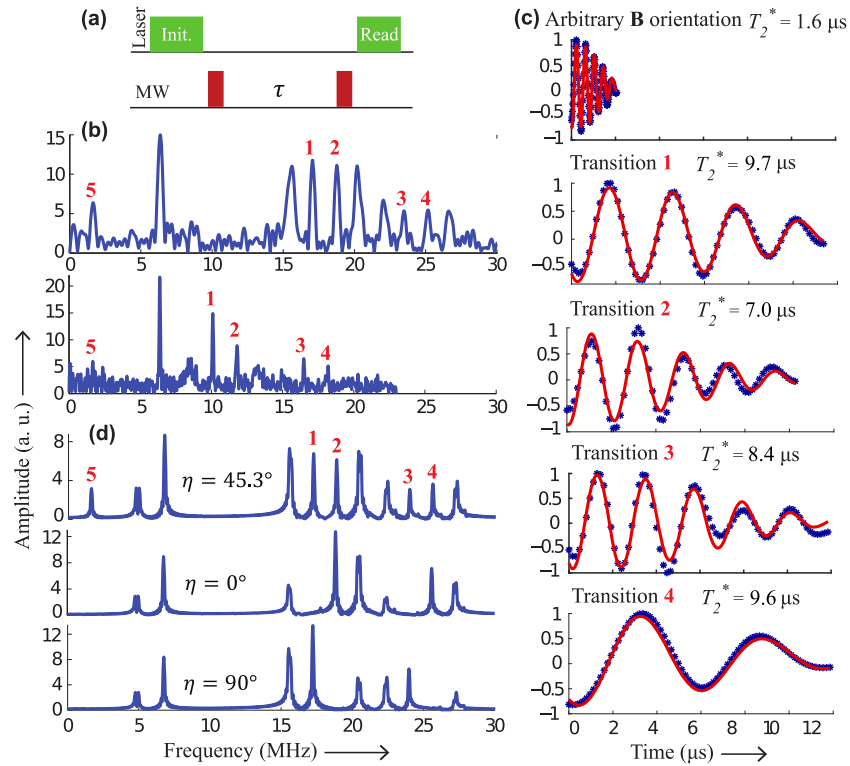


Figure 2. (a) Pulse sequence to measure free induction decays (FIDs). (b) Electron spin resonance (ESR) spectra measured between the energy levels of figure 1(c). For the upper and lower spectra, the detuning frequencies (ν_d) were 20 and 13 MHz, and the FID measurement times were 3 and 12 μs respectively. (c) FIDs of the transitions 1–4 along with that of an electron spin transition at an arbitrary \mathbf{B} -field orientation. Blue stars are the data obtained by inverse Fourier transforming the corresponding spectral lines and the red solid lines fit this data to the equation $a \cos(2\pi\nu t) \exp[-(t/T_2^*)^n]$. (d) Simulated ESR spectra for different values of η of the MW field. The detuning frequency (ν_d) was 20 MHz for the simulation. The frequency of the MW pulses was 2876.8 MHz for both experiment and simulation.

vanishingly small, i.e., $\frac{\partial\nu_i}{\partial B} \approx \frac{\partial\nu_i}{\partial\theta} \approx \frac{\partial\nu_i}{\partial\phi} \approx 0$. This is known as ZEFOZ shift [31–34]. The $m_S = 0$ spin sublevels in figure 1(c) vary slightly with θ (and B) which is due to the transverse components of the electron spin Zeeman and hyperfine interactions.

Another interesting aspect of these transitions is that they can be excited only by individual Cartesian components of the MW or RF field. For the transitions marked by the letter ‘Y’ (green arrows) in figure 1(d), $|\langle\psi_2|S_y|\psi_3\rangle| = 0.80$ and $|\langle\psi_1|S_y|\psi_3\rangle| = 0.59$ and the corresponding matrix elements of the operators S_x and S_z are close to zero (0.02). This implies that these transitions can be excited only by the y -component of the MW field. Note that from the eigenstates of equation (3), the transition amplitudes, $|\langle\psi_2|S_y|\psi_3\rangle| = |\langle\psi_1|S_y|\psi_3\rangle| \approx \frac{1}{\sqrt{2}}$. The actual difference between these quantities is due to the deviations from the approximations in equation (3). Similarly, for the transitions marked by the letter ‘X’ (blue arrows) in figure 1(d), $|\langle\psi_2|S_x|\psi_4\rangle| = 0.79$ and $|\langle\psi_1|S_x|\psi_4\rangle| = 0.60$ and the corresponding matrix elements of the operators S_y and S_z are close to zero (0.02). This implies that these transitions can be excited only by the x -component of the MW field. For the transition marked by the letter ‘Z’ (Red arrow) in figure 1(d), $|\langle\psi_3|S_z|\psi_4\rangle| = 1.0$ and $|\langle\psi_3|S_x|\psi_4\rangle| = |\langle\psi_3|S_y|\psi_4\rangle| = 0$, which implies that this transition can be excited only by the z -component of the RF field. So, in principle, by comparing the experimental transition amplitudes of these transitions, vector detection of applied RF and MW fields can be performed.

In the following, we discuss the experiments performed at this LAC.

Decoherence-free subspaces: To measure the coherence times (T_2^*) of the transitions discussed above, we recorded the optically detected ESR spectra at the corresponding magnetic field orientation ($\theta = 38.4^\circ$). First, FIDs were measured by using the Ramsey sequence shown in figure 2(a), which were then Fourier transformed to get the frequency domain spectra. The phase of the second MW pulse of the Ramsey sequence was varied with respect to that of the first one as $\varphi = -2\pi\nu_d\tau$, i.e. as a linear function of the delay τ between the pulses. The result is a shift in the measured spectra by an artificial detuning ν_d . With this method, the excitation occurs resonantly, but the observed signals are shifted away from the zero-frequency region, which reduces the effect of instrumental drifts.

Figure 2(b) shows the ESR spectra measured between the energy levels of figure 1(c). The frequency of the applied MW pulses was 2876.8 MHz. For the upper spectrum, the FID was measured for a duration of

3 μ s and with a frequency detuning ν_d of 20 MHz. The spectral lines in the frequency range 15–30 MHz correspond to the single-quantum electron spin transitions between the $m_s = 0$ and ± 1 spin sublevels. Along with these, two more transitions appear in the spectrum, one at 1.7 MHz and the other at 6.4 MHz. These are zero-quantum transitions, their frequencies are unaffected by the detuning ν_d [37, 42, 43]. The spectral line that appears at 1.7 MHz corresponds to the transition between the states $|\psi_3\rangle$ and $|\psi_4\rangle$ (marked by the thick red arrow in figure 1(d)), i.e., it belongs to the $m_s = \pm 1$ manifold. The MW pulses do not directly excite this transition and the fluorescence is, in general, not sensitive to population changes within the $m_s = \pm 1$ manifold. Yet, this transition appears in the spectrum which can be explained by considering $|\psi_3\rangle$, $|\psi_4\rangle$ and $|\psi_2\rangle$ (or $|\psi_1\rangle$) as a V-type three level system [37, 44, 45]. The transitions between the states $|\psi_2\rangle$ and $|\psi_3\rangle$, and $|\psi_2\rangle$ and $|\psi_4\rangle$ are labeled as ‘1’ and ‘2’ respectively. Since the transitions 1 and 2 share a common energy level $|\psi_2\rangle$, simultaneous excitation of them by the applied MW pulses create a superposition of the states $|\psi_3\rangle$ and $|\psi_4\rangle$ [46]. The observed fluorescence also gets modulated by the frequency difference between the states $|\psi_3\rangle$ and $|\psi_4\rangle$ due to the quantum interference between the transitions 1 and 2. This phenomenon is known as quantum beats [47–50]. The beat frequency is exactly equal to the frequency difference between the states $|\psi_3\rangle$ and $|\psi_4\rangle$ and its amplitude depends mainly on the excitation amplitudes of the transitions 1 and 2. The spectral line that appears at 6.4 MHz corresponds to the transition between the states $|\psi_1\rangle$ and $|\psi_2\rangle$, i.e., a ^{13}C nuclear spin transition within the $m_s = 0$ manifold. The appearance of this transition in the spectrum can be explained similar to the 1.7 MHz transition by considering $|\psi_1\rangle$, $|\psi_2\rangle$, and $|\psi_3\rangle$ (or $|\psi_4\rangle$) as a Λ -type three level system.

For the lower spectrum of figure 2(b), the FID was measured for a duration of 12 μ s and with a frequency detuning (ν_d) of 13 MHz. The single quantum transitions correspondingly shift by 7 MHz compared to those in the upper spectrum, whereas the zero-quantum transitions do not. The spectral lines labeled by the numbers 1–5 in both spectra correspond to the five electron spin transitions marked in figure 1(d). By comparing the two spectra of figure 2(b), it is clear that the transitions labeled by 1–4 have long coherence times (T_2^*) compared to all the other electron spin transitions. As discussed earlier, this is due to the ZEFOZ shift at the LAC.

To quantify the T_2^* of these four transitions, selective FIDs of them were obtained by inverse Fourier transforming the corresponding spectral lines. These are shown in figure 2(c) in comparison with that of an electron spin transition at an arbitrary magnetic field orientation, which does not have any LAC. The T_2^* of this transition was measured to be 1.6 (± 0.1) μ s and for the transitions 1–4 the values are 9.7 (± 0.5), 7.0 (± 0.9), 8.4 (± 0.8), and 9.6 (± 0.5) μ s respectively. This corresponds to an extension of the coherence time by factors of 5–6.

Vector detection of the MW field: For this, we need to determine the strength (B_{mw}) and orientation (angles ζ and η) of the MW field. First, we determine the azimuthal angle (η) of the MW field, which is the angle between the transverse component of the MW field and the x -axis of the NV center. The spectral lines labeled by 1 and 3 in figure 2(b) correspond to the transitions between the states $|\psi_2\rangle$ and $|\psi_3\rangle$, and $|\psi_1\rangle$ and $|\psi_3\rangle$ respectively. As discussed earlier, they can be excited only by the y -component of the MW field. Similarly, the spectral lines 2 and 4 correspond to the transitions between the states $|\psi_2\rangle$ and $|\psi_4\rangle$, and $|\psi_1\rangle$ and $|\psi_4\rangle$, respectively and they can be excited only by the x -component of the MW field. Therefore, from the amplitudes I_α ($\alpha = 1, 2, 3, 4$) of the lines 1, ..., 4, the angle, η can be determined as follows

$$|\tan \eta| = \sqrt{\frac{I_1}{I_2}} = \sqrt{\frac{I_3}{I_4}}. \quad (4)$$

For our experimental data, we found $\eta = 45.3^\circ$ ($\pm 1.3^\circ$). To test our analysis, we numerically simulated spectra for different values of η . Figure 2(d) shows the resulting spectra. The top trace, which corresponds to $\eta = 45.3^\circ$ matches the experimental spectrum very well. The middle and bottom traces were simulated for $\eta = 0^\circ$ and 90° respectively. In the middle trace the transitions 1 and 3 are absent whereas in the bottom trace the transitions 2 and 4 are absent. Also, in both of them, the spectral line 5, which corresponds to the electron spin RF transition (1.7 MHz) marked by thick red arrow in figure 1(d), is absent. This is expected, because when $\eta = 0^\circ$ or 90° , the MW pulse cannot simultaneously excite the two transitions (1 and 2 or 3 and 4) connecting the two energy levels of this RF transition with the same $m_s = 0$ energy level as one of them has zero transition amplitude.

As discussed earlier, the transitions 1 ($|\psi_2\rangle \leftrightarrow |\psi_3\rangle$) and 5 ($|\psi_3\rangle \leftrightarrow |\psi_4\rangle$) can be excited only by the y - and z -components of the MW and RF fields respectively. This can be used to determine the polar angle (ζ) of the MW field, which is the angle between the MW field and the z -axis of the NV center. For this, we measured the selective Rabi frequencies of the transitions 1 and 5, which are 0.44 (for an MW power of 4.72 mW) and 0.36 MHz (for an RF power of 0.67 mW) respectively. The corresponding expressions can be written as

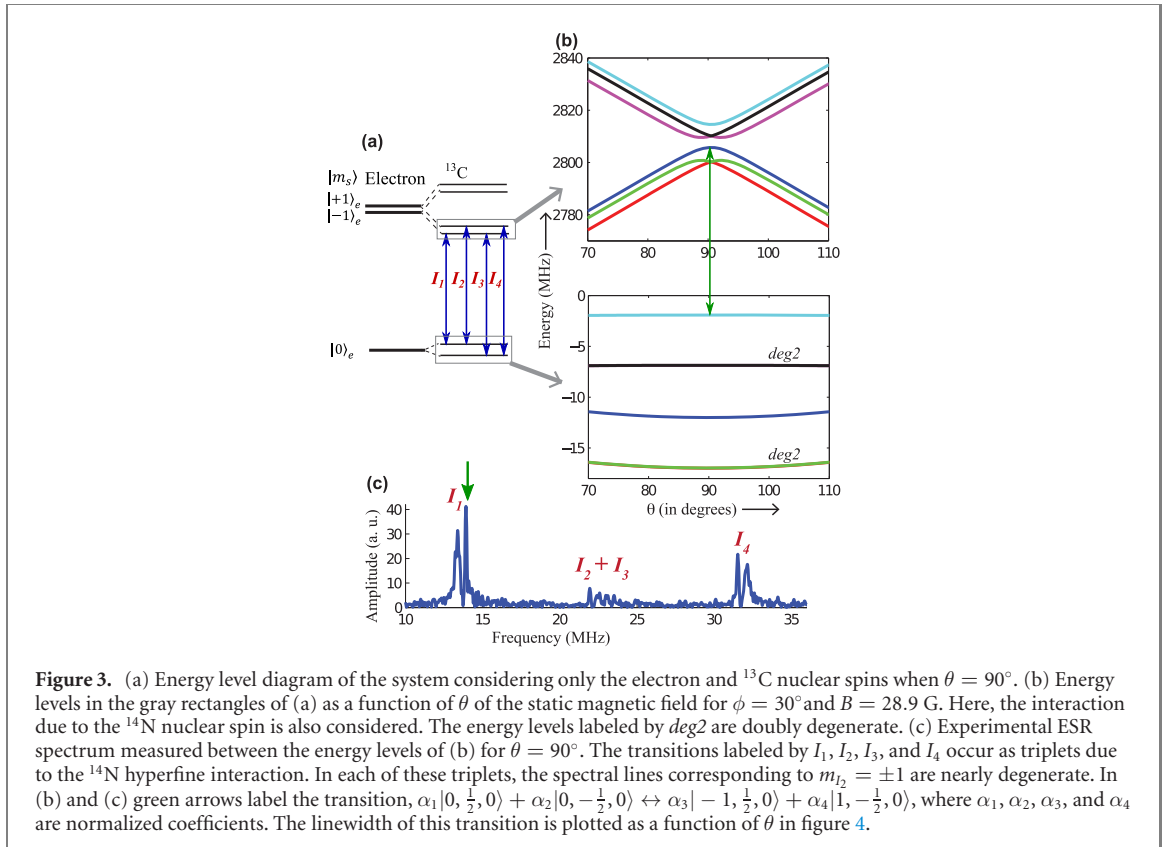


Figure 3. (a) Energy level diagram of the system considering only the electron and ^{13}C nuclear spins when $\theta = 90^\circ$. (b) Energy levels in the gray rectangles of (a) as a function of θ of the static magnetic field for $\phi = 30^\circ$ and $B = 28.9$ G. Here, the interaction due to the ^{14}N nuclear spin is also considered. The energy levels labeled by $\text{deg}2$ are doubly degenerate. (c) Experimental ESR spectrum measured between the energy levels of (b) for $\theta = 90^\circ$. The transitions labeled by I_1, I_2, I_3 , and I_4 occur as triplets due to the ^{14}N hyperfine interaction. In each of these triplets, the spectral lines corresponding to $m_{l_2} = \pm 1$ are nearly degenerate. In (b) and (c) green arrows label the transition, $\alpha_1|0, \frac{1}{2}, 0\rangle + \alpha_2|0, -\frac{1}{2}, 0\rangle \leftrightarrow \alpha_3|-1, \frac{1}{2}, 0\rangle + \alpha_4|1, -\frac{1}{2}, 0\rangle$, where $\alpha_1, \alpha_2, \alpha_3$, and α_4 are normalized coefficients. The linewidth of this transition is plotted as a function of θ in figure 4.

$$\sqrt{2}\gamma_e B_{\text{mw}} \sin \zeta \sin \eta |\langle \psi_2 | S_y | \psi_3 \rangle| = 0.44,$$

$$\sqrt{2}\gamma_e B_{\text{rf}} \cos \zeta |\langle \psi_3 | S_z | \psi_4 \rangle| = 0.36.$$

Taking the ratios of these two expressions and substituting the values of η and the transition amplitudes ($|\langle \psi_2 | S_y | \psi_3 \rangle| = 0.80$ and $|\langle \psi_3 | S_z | \psi_4 \rangle| = 1.0$), we get, $\tan \zeta = 2.15 \frac{B_{\text{rf}}}{B_{\text{mw}}}$. The angle ζ was determined by replacing the ratio, $\frac{B_{\text{rf}}}{B_{\text{mw}}}$ with the corresponding ratio of square roots of measured MW and RF power levels. This value is $\zeta = 39^\circ(-3^\circ, +4^\circ)$. The MW and RF power levels were measured before the diamond sample. After determining the angles, ζ and η , it is possible to determine the amplitudes of the MW and RF fields. From our data, we obtained them as $0.31 (\pm 0.03)$ and $0.12 (\pm 0.01)$ G, respectively.

4. Transverse field induced LAC

Now, consider the LACs that occur in the $m_s = \pm 1$ manifold when the static magnetic field is oriented in the transverse plane of the NV center, i.e., $\theta = 90^\circ$. In contrast to the LACs analyzed in the previous section which occur only for NV centers coupled to a first-shell ^{13}C nuclear spin, transverse field induced LACs occur for all NV centers. The corresponding energy level diagram of the system considering only the electron and ^{13}C nuclear spins is shown in figure 3(a). The energy levels marked by gray rectangles are plotted as a function of the azimuthal angle θ of the static magnetic field in figure 3(b), where the interaction due to the ^{14}N nuclear spin is also included. From this plot, it is clear that LACs occur in the $m_s = \pm 1$ manifold when $\theta = 90^\circ$. The ESR spectrum measured between these energy levels for $\theta = 90^\circ$ and $\phi = 30^\circ$ is shown in figure 3(c).

Decoherence free subspaces: Due to the ZEFOZ shift, the spectral lines have long coherence times (T_2^*) when the B -field is oriented in the xy -plane, compared to other orientations. To compare and quantify the coherence times, we measured the line widths (full width at half height) of the transition marked by green arrow in figure 3(c) as a function of θ of the static magnetic field.

The results are shown in figure 4. The line widths (of the absolute value spectra) are in the range 0.60 to 0.80 MHz except when θ is in between 85 to 95°, where the line width decreases sharply and reaches a minimum of 0.12 MHz at $\theta = 90^\circ$. This shows that when the static magnetic field is oriented in the transverse plane, the line width decreases by 5–7 times and hence the coherence time (T_2^*) increases by the same order. Similar T_2^* improvement has been reported in reference [51] for an NV center without any first-shell ^{13}C nuclear spin. The LACs discussed in this section are due to the transverse magnetic field and

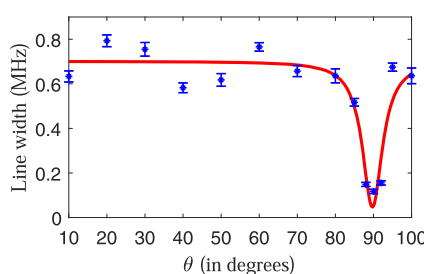


Figure 4. Line width of the transition, $\alpha_1|0, \frac{1}{2}, 0\rangle + \alpha_2|0, -\frac{1}{2}, 0\rangle \longleftrightarrow \alpha_3|-\frac{1}{2}, 0\rangle + \alpha_4|1, -\frac{1}{2}, 0\rangle$ (marked by the green arrows in figure 3), as a function of θ of the static magnetic field. The blue stars represent the experimental data and the error bars represent the standard deviation in the measurement of line widths. The red solid line is a Lorentzian fit, $-a \frac{b}{(x-x_0)^2+b^2} + c$, to the experimental data with parameters $x_0 = 89.7 (\pm 1.0)$, $b = 3.2 (\pm 1.7)$, and $c = 0.7 (\pm 0.07)$.

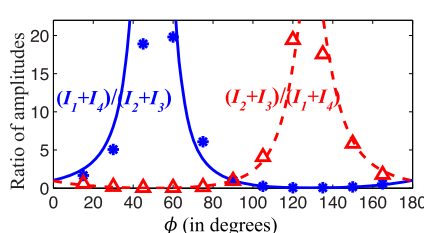


Figure 5. Ratios of amplitudes of spectral lines as a function of ϕ of the static magnetic field for $\theta = 90^\circ$. Blue stars and red triangles represent the experimentally measured quantities, blue solid and red dashed lines represent the corresponding simulated quantities.

occur also in NV centers without any proximal ^{13}C nuclear spin while the nuclear spin induced LACs discussed in section 3 are specific to an NV center with a ^{13}C nucleus in its first coordination shell. It is interesting that the T_2^* improvements observed in both cases are very similar.

It has been theoretically predicted [16] that for single NV centers, whose spin bath is dominated by ^{13}C nuclear spins, T_2 is longest when $\theta = 0^\circ$ and shortest at $\theta = 90^\circ$. Experimental observations [18] on ensembles of NV centers in high-purity diamond crystals with natural abundance ^{13}C concentration supported these predictions. This is in contrast to the behavior of T_2^* observed in this work. This implies that the behaviors of T_2 and T_2^* with respect to magnetic field orientation are very different if the spin bath is dominated by ^{13}C nuclear spins. Interestingly, the behavior of line width versus θ of figure 4 is very similar to the behavior of $1/T_2$ versus θ in reference [52]. There, for similar magnetic field strengths, T_2 of ensembles of NV centers was studied as a function of the polar angle θ of the magnetic field in a diamond sample with a high concentration (≈ 100 ppm) of substitutional nitrogen (p1), where the spin bath is dominated by the electron spins. An improvement in T_2 by 2 times was reported when $\theta = 90^\circ$. It would be interesting to further investigate the similarity of these two cases and if the underlying mechanisms are related.

Determining the azimuthal angle (η) of the MW field: The angle η can also be determined by using the probabilities of the transitions between the $m_S = 0$ and $m_S = \pm 1$ subspaces, labeled as I_1 , I_2 , I_3 , and I_4 in figure 3, for different orientations of the static magnetic field in the transverse plane [37]. The probabilities I_1 , I_2 , I_3 , and I_4 depend on the azimuthal angles, ϕ and η , of the static and MW fields. These probabilities oscillate as a function of ϕ and the phase of these oscillations depends on the value of η [37], i.e., for what values of ϕ , I_1 and I_4 (I_2 and I_3) reaches maxima (minima) depend on the value of η . Therefore, by measuring the intensities of these transitions as a function of ϕ and comparing them with the corresponding numerically calculated transition probabilities, we should be able to determine the value of η . From the measured intensities of the spectral lines, the quantities $(I_1 + I_2)/(I_2 + I_3)$ and $(I_2 + I_3)/(I_1 + I_4)$ are calculated and plotted in figure 5. The corresponding numerical quantities, which are calculated by using $\eta = 45.3$, are also plotted in figure 5. The theoretical quantities are in very good agreement with the experimental ones which reaffirms the value of η determined in the last section.

The azimuthal angle (η) of the MW field with respect to the atomic structure of the center has been determined at both LACs and good agreement between them shows that it is determined accurately. However, the accuracy of the measured polar angle (ζ) is limited. This is mainly due to the impedance mismatches in the MW circuit caused by the copper wire attached to the diamond surface through which the MW fields are generated. These impedance mismatches cause transmitted MW and RF power levels to

depend on the frequency and therefore lead to errors in the ratio $\frac{B_{rf}}{B_{mw}}$, which is used to calculate the polar angle. We expect that a better impedance matching of the MW circuit or a more precise calibration of the RF and MW field strengths could result in more accurate values of the polar angle.

5. Conclusion

We have studied, experimentally and theoretically, two energy LACs of an NV center in diamond coupled to a first-shell ^{13}C nuclear spin in a small static magnetic field. These anti-crossings occur in the $m_s = \pm 1$ manifold due to the strong non-secular components of the Hamiltonian for two different static magnetic field orientations: (i) When the energy level splitting due to the Zeeman interaction of the electron spin is equal to the splitting due to the hyperfine interaction of the ^{13}C nuclear spin (≈ 127 MHz). (ii) When the magnetic field is oriented in the transverse plane of the NV center. At both of these LACs, we observed decoherence free subspaces due to the ZEFOZ shift, resulting in coherence times (T_2^*) of some of the transitions up to 7 times longer than those at other orientations of the magnetic field. At these LACs, some of the electron spin transition amplitudes are dominated by a single component of the magnetic dipole moment. We have used this to perform vector detection of the MW magnetic field by a single NV center. Determining the orientation of the MW field is important to precisely control the NV center using optimal control techniques as the center is not symmetric with respect to the NV axis due to the presence of ^{13}C atom in the first-shell.

Acknowledgments

We thank Jingfu Zhang for useful discussions. This work was supported by the DFG through Grant No. Su 192/31-1. This work was supported by the European Union's Horizon 2020 research and innovation programme under Grant Agreement No. 828946. The publication reflects the opinion of the authors; the agency and the commission may not be held responsible for the information contained in it.

References

- [1] Doherty M W, Manson N B, Delaney P, Jelezko F, Wrachtrup J and Hollenberg L C L 2013 *Phys. Rep.* **528** 1
- [2] Childress L and Hanson R 2013 *MRS Bull.* **38** 134
- [3] Hong S, Grinolds M S, Pham L M, Sage D L, Luan L, Walsworth R L and Yacoby A 2013 *MRS Bull.* **38** 155
- [4] Schirhagl R, Chang K, Loretz M and Degen C L 2014 *Annu. Rev. Phys. Chem.* **65** 83
- [5] Rondin L, Tetienne J-P, Hingant T, Roch J-F, Maletinsky P and Jacques V 2014 *Rep. Prog. Phys.* **77** 056503
- [6] Suter D and Jelezko F 2017 *Prog. Nucl. Magn. Reson. Spectrosc.* **98–99** 50
- [7] Ryan C A, Hodges J S and Cory D G 2010 *Phys. Rev. Lett.* **105** 200402
- [8] de Lange G, Wang Z H, Ristè D, Dobrovitski V V and Hanson R 2010 *Science* **330** 60
- [9] van der Sar T *et al* 2012 *Nature* **484** 82
- [10] Shim J H, Niemeyer I, Zhang J and Suter D 2012 *Europhys. Lett.* **99** 40004
- [11] Zhang J, Souza A M, Brandao F D and Suter D 2014 *Phys. Rev. Lett.* **112** 050502
- [12] Zhang J and Suter D 2015 *Phys. Rev. Lett.* **115** 110502
- [13] Bar-Gill N, Pham L, Jarmola A, Budker D and Walsworth R 2013 *Nat. Commun.* **4** 1743
- [14] Abobeih M H, Cramer J, Bakker M A, Kalb N, Markham M, Twitchen D J and Taminiau T H 2018 *Nat. Commun.* **9** 2552
- [15] Bradley C E, Randall J, Abobeih M H, Berrevoets R C, Degen M J, Bakker M A, Markham M, Twitchen D J and Taminiau T H 2019 *Phys. Rev. X* **9** 031045
- [16] Maze J R, Taylor J M and Lukin M D 2008 *Phys. Rev. B* **78** 094303
- [17] Mizuochi N *et al* 2009 *Phys. Rev. B* **80** 041201
- [18] Stanwix P L *et al* 2010 *Phys. Rev. B* **82** 201201
- [19] Balasubramanian G *et al* 2009 *Nat. Mater.* **8** 383
- [20] Childress L, Gurudev Dutt M V, Taylor J M, Zibrov A S, Jelezko F, Wrachtrup J, Hemmer P R and Lukin M D 2006 *Science* **314** 281
- [21] Dutt M V G, Childress L, Jiang L, Togan E, Maze J, Jelezko F, Zibrov A S, Hemmer P R and Lukin M D 2007 *Science* **316** 1312
- [22] Taminiau T H, Cramer J, van der Sar T, Dobrovitski V V and Hanson R 2014 *Nat. Nanotechnol.* **9** 171
- [23] Neumann P *et al* 2008 *Science* **320** 1326
- [24] Maurer P C *et al* 2012 *Science* **336** 1283
- [25] Shim J H, Niemeyer I, Zhang J and Suter D 2013 *Phys. Rev. A* **87** 012301
- [26] Jelezko F, Gaebel T, Popa I, Domhan M, Gruber A and Wrachtrup J 2004 *Phys. Rev. Lett.* **93** 130501
- [27] He X-F, Manson N B and Fisk P T H 1993 *Phys. Rev. B* **47** 8809
- [28] Epstein R J, Mendoza F M, Kato Y K and Awschalom D D 2005 *Nat. Phys.* **1** 94
- [29] Jacques V *et al* 2009 *Phys. Rev. Lett.* **102** 057403
- [30] Smeltzer B, McIntyre J and Childress L 2009 *Phys. Rev. A* **80** 050302
- [31] Fraval E, Sellars M J and Longdell J J 2004 *Phys. Rev. Lett.* **92** 077601
- [32] Fraval E, Sellars M J and Longdell J J 2005 *Phys. Rev. Lett.* **95** 030506
- [33] Longdell J J, Alexander A L and Sellars M J 2006 *Phys. Rev. B* **74** 195101
- [34] Lovrić M, Glasenapp P, Suter D, Tumino B, Ferrier A, Goldner P, Sabooni M, Rippe L and Kröll S 2011 *Phys. Rev. B* **84** 104417

- [35] Loubser J H N and van Wyk J A 1978 *Rep. Prog. Phys.* **41** 1201
- [36] Felton S, Edmonds A M, Newton M E, Martineau P M, Fisher D, Twitchen D J and Baker J M 2009 *Phys. Rev. B* **79** 075203
- [37] Rao K R K and Suter D 2016 *Phys. Rev. B* **94** 060101
- [38] Wang P *et al* 2015 *Nat. Commun.* **6** 6631
- [39] Shin C S, Butler M C, Wang H-J, Avalos C E, Seltzer S J, Liu R-B, Pines A and Bajaj V S 2014 *Phys. Rev. B* **89** 205202
- [40] He X-F, Manson N B and Fisk P T H 1993 *Phys. Rev. B* **47** 8816
- [41] Chen M, Hirose M and Cappellaro P 2015 *Phys. Rev. B* **92** 020101
- [42] Rao K R K and Suter D 2017 *Phys. Rev. A* **95** 053804
- [43] Shim J H, Nowak B, Niemeyer I, Zhang J, Brandao F D and Suter D 2013 arXiv:[1307.0257](https://arxiv.org/abs/1307.0257) [quant-ph]
- [44] Zhang J, Hegde S S and Suter D 2019 *Phys. Rev. Appl.* **12** 064047
- [45] Hegde S S, Zhang J and Suter D 2020 *Phys. Rev. Lett.* **124** 220501
- [46] Niemeyer I *et al* 2013 *New J. Phys.* **15** 033027
- [47] Forrester A T, Gudmundsen R A and Johnson P O 1955 *Phys. Rev.* **99** 1691
- [48] Dodd J N, Kaul R D and Warrington D M 1964 *Proc. Phys. Soc.* **84** 176
- [49] Hadeishi T and Nieremberg W A 1965 *Phys. Rev. Lett.* **14** 891
- [50] Haroche S, Paisner J A and Schawlow A L 1973 *Phys. Rev. Lett.* **30** 948
- [51] Dolde F *et al* 2011 *Nat. Phys.* **7** 459
- [52] Shin C S, Avalos C E, Butler M C, Wang H-J, Seltzer S J, Liu R-B, Pines A and Bajaj V S 2013 *Phys. Rev. B* **88** 161412